BIOLOGICAL SCIENCES

CLATHRIN LIGHT CHAIN DIVERSITY REGULATES BUDDING EFFICIENCY IN VITRO AND SYNAPTIC VESICLE FORMATION IN VIVO

Lisa Redlingshöfer[1, 2], Faye McLeod[3], Marine D. Camus[1, 2], Yu Chen[1, 2], Jemima J. Burden[4], Ernest Palomer[3], Kit Briant[1, 2], Philip N. Dannhauser[1, 2], Patricia C. Salinas[3] and Frances M. Brodsky[1, 2*]

[1] Research Department of Structural and Molecular Biology, Division of Biosciences, University College London, Gower Street, London WC1E 6BT, UK

[2] Institute of Structural and Molecular Biology, Birkbeck and University College London, Malet Street, London WC1E 7HX, UK

[3] Research Department of Cell and Developmental Biology, Division of Biosciences, University College London, Gower Street, London WC1E 6BT, UK

[4] Medical Research Council Laboratory for Molecular Cell Biology, University College London, Gower Street, London WC1E 6BT, UK

*to whom correspondence should be addressed:
Professor Frances M. Brodsky
f.brodsky@ucl.ac.uk

ABSTRACT

Clathrin light chain (CLC) subunits in vertebrates are encoded by paralogous genes *CLTA* and *CLTB* and both gene products are alternatively spliced in neurons. To understand how this CLC diversity influences neuronal clathrin function, we characterised the biophysical properties of clathrin comprising individual CLC variants for correlation with neuronal phenotypes of mice lacking either CLC-encoding gene. CLC splice variants differentially influenced clathrin knee conformation within assemblies, and clathrin with neuronal CLC mixtures was more efficient in membrane budding than clathrin with single neuronal isoforms nCLCa or nCLCb. Correspondingly, electrophysiological recordings revealed that neurons from mice lacking nCLCa or nCLCb were both defective in synaptic vesicle replenishment. Mice with only nCLCb had a reduced synaptic vesicle pool and impaired neurotransmission compared to wild-type mice, while nCLCa-only mice had increased synaptic vesicle numbers, restoring normal neurotransmission. These findings highlight functional differences between the CLC isoforms and show that isoform mixing influences tissue-specific clathrin function in neurons.

KEY WORDS

Clathrin, membrane traffic, coated vesicle formation, protein isoforms, neuronal synapse

SIGNIFICANCE STATEMENT

This study reveals that diversity of clathrin light chain (CLC) subunits alters clathrin properties and demonstrates that the two neuronal CLC subunits work together for optimal clathrin function in synaptic vesicle formation. Our findings establish a role for CLC diversity in synaptic transmission and illustrate how CLC variability expands the complexity of clathrin to serve tissue-specific functions.

52 **INTRODUCTION**

53

54 Clathrin mediates vesicle formation from the plasma membrane and endosomal
55 compartments (1). Recruited by cargo-recognising adaptor proteins, triskelion-shaped
56 clathrin proteins assemble into polyhedral lattices to capture membrane-associated cargo
57 and promote membrane bending into clathrin-coated vesicles (CCVs). Through sequestration
58 of a variety of cargo, CCVs play fundamental roles in general cellular physiology including
59 regulation of nutrient uptake and signalling, as well as in tissue-specific membrane traffic
60 such as synaptic vesicle (SV) generation (2). This range of clathrin functions has been
61 attributed to adaptor and accessory protein variation (3). However, functional diversity is also
62 generated by variability of clathrin subunits. Vertebrates have two types of clathrin heavy
63 chains with distinct functions (4). The major vertebrate clathrin is formed from clathrin heavy
64 chain CHC17 (herein referred to as CHC) associated with clathrin light chains (CLCs), which
65 do not bind the minor CHC22 clathrin isoform. Vertebrate CLCs are encoded by two different
66 genes *CLTA* and *CLTB* (in humans), producing CLCa and CLCb isoforms of about 60%
67 sequence identity (5, 6). Their sequence differences were conserved throughout evolution,
68 after their encoding genes arose through duplication, suggesting the two isoforms can
69 mediate distinct functions (7, 8). Expression levels of the CLCa and CLCb isoforms are
70 tissue-specific (9), and further variation is created by alternative gene splicing during
71 development (10) and in brain (5, 6). Here we address how CLC diversity affects the
72 biophysical properties of clathrin and how the resulting variation affects the specialised
73 function of clathrin in synaptic vesicle (SV) replenishment.

74

75 Limited functional differences between CLCa and CLCb have been observed in cell culture
76 with respect to clathrin dynamics (11), during focal adhesion formation (12) and during
77 cancer cell migration (13), with mechanisms attributed to possible isoform-specific
78 differences in CLC binding proteins and post-translational modification (14). Loss of CLCs in
79 culture and *in vivo* affects CCV uptake of some, but not all cargo, possibly reflecting

variability in mechanical demand for packaging different cargo into CCVs (9, 14, 15). The capacity for biophysical differences in clathrin comprising different CLC isoforms and their splicing variants to influence tissue-specific clathrin functions has not yet been considered. CLC variability has potential to affect clathrin function as CLCs interact with key domains of the clathrin triskelion that contribute to clathrin-mediated membrane bending. They bind the trimerisation domain (TxD) of the triskelion vertex where the three component CHCs interact (16, 17), and extend along the triskelion leg to the bend at the knee where CLCs regulate conformation (18). Like various other endocytic proteins (3), CLCs undergo neuron-specific splicing (19), which introduces one exon in CLCb (encoding 18 residues) and two exons (encoding 30 residues) in CLCa at equivalent positions near the CLC C-termini, resulting in higher molecular weight forms nCLCb and nCLCa (5, 6), and suggests neuron-specific functions for these variants. *In vitro*, CLCs are required for efficient clathrin-mediated membrane vesiculation at low temperature (20). Thus, CLCs could affect clathrin-mediated membrane deformation directly through their influence on clathrin lattice properties (20, 21), as well as indirectly through cellular interaction with proteins that influence the actin cytoskeleton (22-25).

SV replenishment by membrane traffic following neuronal degranulation is critical for sustained neurotransmission. Endocytosis is required to regulated synaptic plasma membrane surface area and to retrieve SV proteins (26), and SVs are generated from the plasma membrane and endosome-like compartments (27). The essential sites of clathrin function in these pathways are debated (2, 28), but dysfunction of clathrin-associated endocytic proteins is associated with neurological defects observed in Parkinson's disease (29), Alzheimer's disease (3) and in numerous animal models in which such proteins have been genetically deleted (30-35).

Here, we assess how clathrin lattices formed with neuronal and non-neuronal CLC variants could differentially affect function by correlating their *in vitro* biophysical properties with *in*

108 *vivo* neuronal phenotypes of mice lacking CLC-encoding genes. We found that CLC
109 composition significantly influenced clathrin lattice properties and their ability to form vesicles
110 from liposome membrane *in vitro*. CLC splice variation influenced assembly curvature by
111 regulating CHC knee conformation, resulting in decreased ability of individual neuronal splice
112 variants to deform membrane *in vitro*. This effect was ameliorated for lattices formed from a
113 mixture of neuronal CLC isoforms. Mice lacking either CLCa or CLCb isoforms showed
114 corresponding differences in SV replenishment and synaptic neurotransmission compared to
115 their wild-type (WT) littermates expressing both isoforms, and to each other. Collectively,
116 these functional differences between CLC isoforms observed *in vitro* and *in vivo* establish a
117 role for CLC diversity in regulating clathrin function in neurons.
118

RESULTS

CLC splice variants differentially influence lattice curvature via the triskelion knee

Within clathrin lattices, the knee bending angle determines whether a hexagon (non-curvature inducing) or pentagon (curvature-inducing) is formed (36). In addition, the characteristic pucker at the triskelion vertex and the crossing angle of interacting CHC legs can further modulate lattice curvature (37, 38) (Fig. 1a). This versatility of clathrin assemblies allows clathrin to sequester cargo of various sizes as well as to form stable, flat assemblies that serve as signalling hubs (3, 39). For each closed cage, there is a fixed number of 12 pentagons, but a varying number of hexagons (40) (Fig. 1a). Thus, larger cages (i.e. lattices of lower curvature) have a smaller pentagon to hexagon ratio. CLCs maintain the puckered conformation of triskelia in flat assemblies (20) and structural studies showed that nCLCb can influence conformation of the triskelion knee up to a degree that inhibits assembly (18). Considering these effects on CHCs, we hypothesized that sequence differences between the CLC isoforms and alterations due to splicing might modulate CLC influence on triskelion conformation and lattice curvature.

To address this, we produced clathrin triskelia of defined CLC composition by reconstituting tissue-derived CHC triskelia with recombinantly expressed CLCa, CLCb, nCLCa or nCLCb (Fig. S1a-d) (41). We then induced assembly of these different clathrins into closed cages and analysed their diameters as a measure of lattice curvature by electron microscopy. Previous studies showed that tissue-derived, CLC-bound clathrin (native) forms two major size classes, while CHC-only triskelia predominantly form small-sized cages (42-45). Our results confirmed that without CLCs, CHC formed predominantly cages of less than 90 nm in diameter with an average size of around 70 nm, representing cages of up to 60 triskelia (44). Clathrin with each of the CLC variants was further able to form larger cages with an average diameter of around 110 nm (140 triskelia) for those cages. The degree to which larger cages

146 were formed varied significantly between splice variants (Fig. 1b, c), indicating that the
147 neuronal splice inserts regulate the influence of CLCs on lattice curvature.
148
149 To establish whether differences in larger cage formation resulted from CLC influence on the
150 triskelion vertex or on the CHC knee conformation or both, we dissected the effect of CLCs
151 separately for each domain. To test whether CLC diversity exerts influence through varying
152 CHC knee conformation, we produced clathrin cages from two CHC fragments that together
153 constitute a full-length clathrin triskelion “cut” at the knee (Fig. 1d) (46). The Hub fragment
154 (residues 1074-1675) was reconstituted with different CLCs (47) and combined with the
155 terminal-distal leg segment (TDD, residues 1-1074, Fig. S1e) under conditions promoting
156 their co-assembly (46). Cages produced when TDD was combined with CLC-reconstituted
157 Hub fragments were similar in size to fragment cages without CLCs, and the larger cages
158 observed for CLC variants associated with intact CHC did not form (Fig. 1d, e). This result
159 demonstrates that for CLC diversity to exert an effect on lattice curvature, the CHC knee
160 must be intact, and shows that CLC splice variants differ in their influence on CHC knee
161 conformation. Formation of larger cages by neuronal CLCs suggests that the neuronal splice
162 inserts reduce the likelihood of knee conformation favouring pentagon formation and support
163 hexagon formation. To establish whether cage size differences also correlated with CLC
164 effects at the TxD, the different CLCs were compared for their ability to stabilise the TxD (Fig.
165 S2) in an assay that measures triskelion dissociation. While dissociation differences were
166 observed between triskelia reconstituted with the different CLC isoforms and their splice
167 variants, these effects did not correlate with cage size differences, suggesting that CLC
168 influence at the vertex is not a major factor in lattice curvature.
169
170 **CLC diversity modulates mechanical properties of the clathrin lattice**
171 We next investigated whether the influence of CLCs on the CHC knee had mechanical
172 consequences for their ability to support membrane deformation. Mechanical properties of
173 clathrin lattices were previously shown to be CLC-dependent and reduced ability of CLC-free

174 clathrin to bend membranes *in vitro* was correlated with poorer planar lattice quality (20). To
175 establish whether CLC diversity influences lattice quality, clathrins with different CLC
176 composition were assembled on electron microscopy (EM) grids coated with a clathrin-
177 binding fragment of epsin1 (H_6-ΔENTH-epsin$^{144-575}$, Fig. S1f) (48). The flat lattices formed
178 were visualized by EM and their periodicity (quality) assessed by Fourier transform analysis.
179 Lattice quality was significantly reduced for clathrin with the neuronal splice variants of either
180 CLCa or CLCb compared to clathrin reconstituted with their respective non-neuronal variants
181 (Fig. 2a, b). While lattice quality was not significantly different between clathrin with nCLCa or
182 nCLCb, nCLCb clathrin showed a tendency to form lattices of poorer quality (Fig. 2c) and
183 lattice quality was significantly improved if formed from a 1:1 mix of nCLCa clathrin and
184 nCLCb clathrin (Fig. 2b). To visualise the nature of CLC distribution in these mixtures,
185 lattices were generated using His-tagged nCLCa clathrin or nCLCb clathrin combined with
186 the cognate untagged CLC and labelled with Ni-NTA-gold (Figure S3), confirming a uniform
187 distribution of each neuronal CLC within the mixed lattice. In contrast to the behaviour of the
188 neuronal CLCs, lattice quality was reduced in mixtures of CLCa clathrin and CLCb clathrin
189 compared to lattices formed by clathrin with only CLCa or CLCb. Notably, the lattice quality
190 resulting from neuronal and non-neuronal CLC compositions correlated with their influence
191 on cage size (Table 1), and suggests potential differential influence on membrane budding.
192
193 To determine whether CLC-related variation in lattice quality affects membrane bending, as
194 seen for complete absence of CLCs, we tested the function of the CLC-reconstituted
195 clathrins using a low temperature *in vitro* budding assay (20). In this assay, H_6-ΔENTH-
196 epsin$^{144-575}$, coupled to liposomes via modified Ni-NTA lipids, captures clathrin at the
197 liposome surface. Lattice assembly on these liposomes generates buds, which remain
198 attached to the liposome due to lack of dynamin, needed for scission (20, 48). The efficiency
199 of clathrin with different CLC composition to form coated buds was assessed at 15°C, a
200 temperature permissive for budding by native clathrin but reduced for CLC-free clathrin (20).
201 For each clathrin, we measured the diameter of clathrin-coated membrane profiles in thin-

202 section electron micrographs and assessed budding efficiency by the percentage of clathrin-
203 coated buds (defined by a fitted diameter < 200 nm) compared to all clathrin-coated
204 membrane profiles analysed (Fig. 3a). In line with previous findings, we found that at 15°C
205 native clathrin was about twice as efficient in membrane deformation as CLC-free clathrin
206 (20), and that budding efficiencies varied with the CLC composition of clathrin tested (Fig.
207 3b). CLCa or CLCb clathrin lattices vesiculated membrane more efficiently than either
208 neuronal clathrin variant (Fig. 3b), demonstrating that CLC splicing affects budding efficiency.
209 We found no statistically significant differences between CLCa and CLCb isoforms of the
210 neuronal or non-neuronal splice variants over the whole data set, yet differences within each
211 experiment indicate that in budding, clathrin with CLCb may be slightly more efficient than
212 CLCa clathrin, and nCLCb clathrin potentially less efficient than nCLCa clathrin (Fig. 3c).
213 Visualising the clathrin-coated liposomes absorbed to EM grids confirmed that all clathrins
214 tested assembled into intact lattices or buds on the liposome surface (Fig. S4), suggesting
215 that the observed variation in budding efficiency was not due to impaired lattice formation,
216 but CLC-dependent lattice properties. Notably, mixing reconstituted neuronal clathrins
217 significantly improved budding efficiency (Fig. 3d), overall reflecting the same pattern as
218 observed for both lattice quality and curvature (Table 1), suggesting all three parameters
219 result from differential CLC effects at the triskelion knee. Furthermore, all three assays
220 demonstrated that neuronal clathrin benefits from cooperative co-assembly of clathrin with
221 both isoforms.
222
223 Membrane deformation could result either from lattice formation at constant curvature or
224 through transitioning from flat to curved lattices (Fig. 3e). To determine how budding was
225 generated in our *in vitro* system and how it was influenced by CLCs, we measured the angle
226 between the convex side of the coat and the coat-free membrane (Fig. 3e), coat curvature
227 (i.e. diameter of the clathrin-coated structure), coat length and neck width for all coated
228 membrane profiles (49) and then correlated these measurements. We observed a variety of
229 coat curvatures in our system (Fig. 3f) and found that while neck width decreased with

230 budding angle, as would be expected for both modes of deformation, coat curvature and
231 neck width correlated with the budding angle of the coated to the coat-free membrane (Fig
232 3g, i). This indicates that lattices transition from flat to curved in our system, rather than
233 assembling with constant curvature, which would be independent of budding angle (Fig. 3e).
234 In further support of this, we found no correlation between coat length and budding angle
235 (Fig. 3h). Thus, we conclude that in our *in vitro* system, clathrin initially assembles into flat
236 lattices on the liposome membrane and then gradually deforms the underlying membrane
237 into coated buds, as observed by others in human SK-MEL-2 cells (49, 50). Our results
238 suggest that CLC-mediated regulation is required for the transition of flat to curved lattices
239 and that CLC variants differ in their ability to promote this transition. Thus, collectively from
240 these *in vitro* studies, we conclude that CLC variants differentially regulate triskelion knee
241 conformation within the lattice, affecting the mechanical ability to deform membrane into
242 coated buds through varying the probability of pentagon formation via influence on the CHC
243 knee. In particular, single neuronal splice variants were less functional in these properties
244 and lattice quality compared to their non-neuronal splice variants, while a mixture of neuronal
245 variants appeared to improve their functionality to non-neuronal levels.
246

247 **CLC composition affects SV pool size and replenishment**

248 Our *in vitro* experiments indicate that clathrin lattices formed from a mixture of clathrin with
249 each neuronal CLC isoform efficiently support membrane deformation, while clathrin
250 comprising only one neuronal CLC isoform is attenuated for membrane budding. Therefore,
251 we predicted that neurons of animals with only one CLC isoform might be defective in
252 clathrin-mediated pathways that rely on SV formation. This hypothesis was investigated in
253 knock-out (KO) mice lacking the *Clta* or *Cltb* genes in all tissues (CLCa KO and CLCb KO
254 mice). We previously generated CLCa KO mice (9) and have now produced CLCb KO mice.
255 Loss of *Cltb* in CLCb KO mice was confirmed by PCR, and no CLCb or nCLCb protein was
256 detected in all tissues analysed (Fig. S5). Whereas wild-type (WT) mice express a mixture of
257 CLCs in most tissues (9), CLCa KO mice express only CLCb or nCLCb, and CLCb KO mice

258 express only CLCa or nCLCa, enabling functional analysis of clathrin with only one type of
259 CLC in neurons (Fig. 4a).
260
261 Hippocampal neurons have frequently been used to study the function of endocytic proteins
262 in synaptic transmission (27, 30, 31, 33, 34, 51). H&E staining of the hippocampus showed
263 no morphological abnormalities in either KO strain, indicating that absence of either CLC
264 isoform does not affect gross hippocampus development in the CLC KO mice (Fig. S6). We
265 therefore used this system to evaluate the function of mature excitatory synapses in the CA1
266 region of the adult hippocampus, a region of well-defined neuronal architecture and
267 neurophysiological circuitry, in the CLC KO and WT mice. For electrophysiological recordings
268 at Schaffer collateral (SC)-CA1 synapses in acute hippocampal slices, a stimulating
269 electrode was placed in the SC fibres of the CA3 region and responses were then recorded
270 in the CA1 pyramidal cell layer (Fig. 4b).
271
272 To determine the role of CLC diversity in SV pool replenishment *in vivo*, we recorded the
273 responses to a prolonged high-frequency stimulus, which maximally depletes presynaptic
274 terminals of the readily releasable pool (RRP) of SVs (52-54). Under these conditions, initial
275 responses would draw from the pre-existing SV pool, while sustained neurotransmission
276 would rely on the efficiency of SV pool replenishment (53). Using this approach, we were
277 able to assess CLC-dependency for different stages of SV exo- and endocytosis from these
278 recordings. We found that the initial fusion rate of SVs in either KO strain was similar to that
279 of their WT littermates, indicating that correct packaging of fusion-mediating cargo was not
280 affected by changes in CLC composition (Fig. 4c, d and Fig. S7). Instead, both KO models
281 had a decreased SV recycling rate characteristic of a defect in acute SV pool replenishment
282 (Fig. 4c, d). This finding correlated with our expectation from *in vitro* properties of
283 reconstituted clathrin isoforms that showed clathrin lattices with only one type of neuronal
284 CLC were different from mixed lattices in their assembly properties (Table 1).
285

286 Further calculations based on data obtained from sustained trains of action potentials
287 indicated that the RRP was larger in the CLCb KO mice but reduced in the CLCa KO mice
288 when compared to WT littermates (Fig. 4c, d and Fig. S7), revealing a phenotype that we did
289 not expect from our *in vitro* data. To establish whether indeed the SV formation was altered
290 in the CLC KO mice rather than the ability to mobilise SVs from other SV pools, we assessed
291 the ultrastructure of excitatory synapses in the CLC KO mice and their WT littermates (Fig.
292 4e). Indeed, SV density was significantly reduced in hippocampal neurons in the CLCa KO
293 animals. In contrast, SV density in equivalent neurons of the CLCb KO mice was significantly
294 increased compared to their WT littermates (Fig. 4f, j), in line with our RRP estimates from
295 electrophysiological recordings (Fig. 4c, d). Other parameters such as individual SV size
296 (Fig. 4g, k), postsynaptic density (PSD) length (Fig. 4h, l) and excitatory synapse density
297 (Fig. 4i, m) were similar between both KO strains and respective WT littermates. Together,
298 these data show that CLCs are required for efficient and sustained synaptic function and
299 suggest that loss of either CLC decreases acute SV replenishment by affecting immediate
300 formation, correlating with expectations from reduced in vitro budding efficiency, but that the
301 KO strains differ in their ability to generally maintain SV pools. Thus, CLC composition
302 influences SV density in excitatory neurons of the hippocampus and indicates differential
303 functions for nCLCa and nCLCb in SV generation, such that mice with only nCLCa can
304 sustain a compensatory pathway for SV generation and mice with only nCLCb cannot.
305

306 **CLCa KO and CLCb KO mice have distinct neurological and behavioural defects**

307 To further investigate the differential consequences of CLCa or CLCb KO for synapse
308 function, we conducted additional electrophysiological experiments to characterise synaptic
309 transmission in our KO animals. Analyses of the evoked excitatory postsynaptic current
310 (EPSC) responses to stimuli of increasing magnitude revealed decreased EPSC response
311 amplitude in the CLCa KO mice compared to WT littermates, suggesting impaired basal
312 synaptic transmission in the CLCa KO mice (Fig. 5a). In contrast, the evoked EPSC
313 response amplitude in hippocampal slices from the CLCb KO mice was of similar or higher

314 magnitude than that of their WT littermates, suggesting that basal synaptic transmission was
315 intact and even enhanced (Fig. 5b). These differences in synaptic connectivity between
316 hippocampal function in the two KO strains could arise from defects in presynaptic
317 neurotransmitter release correlating with differences in SV pool size in the KO animals
318 relative to their WT littermates (Fig. 4).
319
320 Further, we performed paired-pulse ratio (PPR) recordings experiments, an approach that
321 allows assessment of defects in neurotransmitter release (55, 56). In excitatory neurons such
322 as those analysed here, a second stimulus pulse (P_2) fired in short succession after an initial
323 pulse (P_1) results in a larger response than the first stimulus. This facilitation is dependent on
324 changes in the probability of neurotransmitter release. PPR is inversely correlated with
325 release probability, as lower initial release probability leaves more fusion-competent vesicles
326 remaining at the terminal which are then released after the second stimulus (55, 56). We
327 observed that, compared to WT littermates, the PPR was increased in CLCa KO mice,
328 consistent with a reduction in release probability (Fig. 5c). In contrast, no differences in PPR
329 were observed in CLCb KO mice compared to WT littermates (Fig. 5d). Thus, specific loss of
330 nCLCa impairs presynaptic function compromising neurotransmitter release at the SC-CA1
331 synapse. Collectively, our electrophysiological data supports the morphological data (Fig. 4),
332 indicating that neurons with only nCLCa clathrin can compensate for defective SV
333 regeneration by expanding their SV pool from another pathway, while neurons with only
334 nCLCb clathrin cannot compensate and show decimated SV pools from impaired
335 replenishment.
336
337 Ongoing breeding of the CLCa KO colony confirmed a 50% survival rate compared to that
338 expected for homozygous CLCa KO mice (9), whereas homozygous CLCb KO mice had no
339 survival defects (Fig. 5e). Survival phenotypes similar to the CLCa KO animals have been
340 reported for other genetic deletions in endocytic pathways, which also displayed neuronal
341 phenotypes (30) in the hippocampus and other regions of the brain (32). Thus, we assessed

342 performance in the rotarod test for neuro-motor coordination for both CLC KO mice (57).
343 Compared to their WT littermates, surviving CLCa KO mice displayed defects in rotarod
344 balance, whereas CLCb KO mice did not (Fig. 5f). Further assessment of sensorimotor
345 function revealed that CLCa KO mice exhibited defects in a grid-walking test, (Fig. 5g), but
346 not in grip strength (Fig. 5h), suggesting neurological rather than muscular dysfunction in the
347 CLCa KO animals, supporting the notion that loss of nCLCa is less tolerable than loss of
348 nCLCb. Together, the phenotypes of the KO animals indicate that neuronal CLC isoforms are
349 differentially able to support compensatory mechanisms for adjusting SV pools hippocampal
350 synapses with impaired acute SV replenishment, and suggest that clathrin with only nCLCa
351 is more functional than clathrin with only nCLCb, while a mix of both neuronal CLCs is
352 necessary for optimal clathrin function in neurons, in keeping with their synergistic
353 contribution to clathrin function *in vitro.*
354

355 **DISCUSSION**

356

357 To understand the consequences of CLC diversity for clathrin function, we characterised the
358 biophysical properties of *in vitro* assemblies formed from clathrin comprising single CLC
359 isoforms and correlated these properties with neuronal phenotypes observed in KO animals
360 expressing single CLC isoforms. We found that neuronal CLC splicing affects lattice
361 properties (Fig. 1b and Fig. 2b) by diversifying the CLC influence on the CHC knee to
362 regulate lattice curvature (Fig. 1c, d) and deform membrane (Fig. 3b). In particular, CLC
363 splicing apparently influences clathrin's ability to introduce pentagons in order to transition
364 from flat to curved lattices (Fig. 1a and Fig. 3e-i). Our *in vitro* studies further suggest that
365 lattices formed from mixtures of clathrin with nCLCa and nCLCb have different assembly
366 properties and are more efficient in membrane budding compared to clathrin with only one
367 type of neuronal CLC (Fig. 2b, 3d). Consistent with this observation, neurons from both
368 CLCa and CLCb KO mice showed defects in synaptic transmission that indicated acute
369 clathrin-dependent SV replenishment was impaired (Fig. 4c, d). However, the CLCa KO mice
370 had reduced numbers of SVs in their hippocampal synapses, while the CLCb KO mice had
371 more SVs than their WT littermates (Fig. 4f, j). Thus, although acute SV replenishment was
372 impaired in both KO strains, clathrin with only nCLCa (in the CLCb KO mice) was able to
373 support a compensatory pathway of SV formation, while clathrin with only nCLCb (in the
374 CLCa KO) was not (Fig. 5a-d). These findings establish functional differences between CLC
375 isoforms *in vitro* and *in vivo* and demonstrate how resulting clathrin diversity is important for
376 clathrin function in neurons.

377

378 Neuronal splicing predominates for CLCb in neurons (58), while neuronal CLCs are not
379 present in other brain cells such as glial or Schwann cells (19), indicating that the CLC splice
380 variants segregate within brain cell types to fulfil distinct functions. Neuronal CLC splicing
381 had a significant influence on lattice curvature and budding efficiency, decreasing the
382 likelihood of forming pentagons (Table 1), which was attributable to effects on the CHC knee

383 domain (Fig. 1d). Given that the inserted sequences are located near the TxD where the C-
384 termini of CLCs are bound (arrowheads, Fig. 6a), we propose that the splice inserts affect
385 the conformation of the adjacent knee of a neighbouring triskelion, which is closer than the
386 knee of the triskelion to which the CLC is bound (Fig. 6b). This intermolecular influence could
387 involve splice inserts at the C-terminus (stars, Fig. 6b) interacting with the neighbouring CHC
388 or with the N-terminal domain of a CLC bound to the neighbouring knee (Ns, Fig. 6b).
389 Considering the average 40% sequence differences between CLCa and CLCb isoforms and
390 their even greater variation at the N-terminus, inter-CLC interactions could vary depending
391 on which splice isoform interacts with which CLC isoform N-terminus, thereby influencing
392 overall lattice properties. This imputed interaction may be lost from clathrin with non-neuronal
393 CLCs, which would explain why mixing non-neuronal CLC isoforms does not affect *in vitro*
394 budding to the same extent as mixing neuronal CLC isoforms (Fig. 3d).
395
396 Here, we characterise the properties of homo- and hetero-assemblies of clathrin comprising
397 single CLC isoforms. In brain, CLC isoforms are apparently randomly distributed on triskelia
398 (59), in which case neuronal inserted sequences could still influence lattice curvature via
399 interactions with an adjacent triskelion knee. The presence of nCLCb would serve as an
400 attenuator of nCLCa-specific interactions and vice versa. Further, in cells where CLCb
401 expression is transiently increased (60), newly synthesized triskelia would be generally
402 occupied by a single CLC isoform as clathrin subunit turnover is slow (61). The resulting
403 homotypic clathrins would then participate mixed in lattices, as we have studied here. Thus,
404 neuronal CLC isoform expression ratios (and/or local abundance within cells) could tailor
405 clathrin lattice properties specifically to particular needs.
406
407 There are several pathways involved in SV recycling in neurons and the role of clathrin has
408 been widely debated, possibly because the contribution of each pathway to SV formation is
409 variable between organisms, types of neurons and stimulus (51, 62, 63). SV recycling can
410 either be achieved by direct regeneration of SVs through clathrin-mediated endocytosis from

411 the plasma membrane at low-frequency stimulus, or through clathrin-independent
412 mechanisms, which predominantly mediate retrieval of SV components from the plasma
413 membrane under high stimulus (2, 27, 28, 33, 51). Rapid clathrin-dependent trafficking of SV
414 proteins from the endosomal pathway then leads to re-sorting and formation of SVs at high-
415 frequency stimulus (2), which can occur in a timeframe of 1-3 seconds after stimulation (27).
416 In our analysis of neurotransmission, SV recycling defects were detected by
417 electrophysiology within three seconds at high stimulus (20 Hz for 3s), suggesting the
418 defects detected were due to impaired clathrin-mediated regeneration of SVs from
419 endosomes. These findings are consistent with previously observed roles for CLCs in
420 recycling from non-neuronal endosomal compartments (60, 64).
421
422 That an acute SV pool replenishment defect was shared by neurons in both CLC KO strains
423 fits with our *in vitro* biophysical data that demonstrate single neuronal CLCs are not as
424 efficient in membrane deformation as a mixture of clathrin with both neuronal CLCs (Fig. 3d).
425 In response to this defect, we found that clathrin with only nCLCa generated an increased
426 steady-state SV pool in CLCb KO neurons, while clathrin with only nCLCb could not (Fig.
427 6b). CLCa seems to have preferential connection with the actin cytoskeleton compared to
428 CLCb (12, 24), which might account for the ability of nCLCa clathrin to function on its own
429 without nCLCb and benefit from involvement of actin and its accessory molecules to
430 compensate for defects in acute SV pool replenishment. It is possible that in the (normal)
431 presence of nCLCb, the actin interactions of nCLCa may be “diluted down”, so that nCLCb
432 works as an attenuating balancing mechanism to control SV pools at steady state. The
433 presence of nCLCb would simultaneously create lattice properties for efficient CCV budding
434 during neurotransmission. In its absence, the acute replenishment pathway would decrease
435 in efficiency but loss of the nCLCb attenuation effect enables a compensatory pathway with
436 nCLCa only. Thus, the budding defect resulting from a change in biophysical properties of
437 clathrin is detectable only under acute demand, and when demand is less acute, there are

438 mechanisms by which nCLCa clathrin can generate SVs that are not supported by nCLCb
439 clathrin.
440
441 Considering the whole animal phenotypes, including the increased mortality rate for CLCa
442 but not CLCb KO animals, CLCa seems to be the more functional CLC, while CLCb functions
443 mainly in conjunction with CLCa. This is in line with the observation that CLC expression
444 ratios vary with tissue, and while lymphoid cells almost exclusively express CLCa, no tissue
445 has been found to express exclusively CLCb (9, 61). In addition, CLC isoform splicing
446 changes during cell differentiation, development (10, 58) and ratios of CLCb relative to CLCa
447 are modulated in tumour progression (13) and cell migration (60). These observations, in
448 combination with the *in vitro* and *in vivo* data reported here, support the concept that, in
449 addition to influencing accessory protein interaction, the conserved CLC isoform and splicing
450 differences characteristic of vertebrates facilitate tissue-specific clathrin functions by directly
451 modulating clathrin lattice properties. In particular, CLC diversity regulates clathrin budding
452 efficiency, a property that we show here affects SV formation under acute demand, and is
453 likely to influence other pathways that rely on rapid clathrin-mediated membrane traffic.
454

455 **MATERIALS AND METHODS**

456

457 **Protein expression and purification**

458 CLCs in pET28a were expressed with a thrombin-cleavable, N-terminal His-tag and purified
459 by standard nickel affinity chromatography and further polished by size exclusion
460 chromatography on a Superdex 200 10/300 GL column (GE Healthcare). His-tags of CLC
461 constructs were removed by thrombin cleavage. His-tagged epsin1 in pET32c and His-
462 tagged ΔENTH-epsin$^{144-575}$ in pQE32 were expressed and purified as previously described by
463 standard nickel affinity chromatography and size exclusion chromatography on a Superdex
464 200 10/300 GL column (GE Healthcare) (65).

465

466 CCVs were purified from porcine brain as described previously (45) and clathrin triskelia
467 purified by tris-extraction and size exclusion chromatography on a Superose 6 Increase
468 10/300 GL column (GE Healthcare). To generate CHC-only triskelia, endogenous CLCs were
469 removed using NaSCN and separated from CHC by size exclusion chromatography (41).

470

471 For reconstitution of clathrin of defined CLC composition, CHC in buffer C (50 mM Tris-HCl
472 pH 8.0, 50 mM NaCl, 2mM EDTA, 1mM DTT) at 0.8-1.0 mg/ml was incubated with purified
473 CLCs at 0.7 – 1.0 mg/ml in in the same buffer or in 20 mM Tris-HCl pH 8.0, 200 mM NaCl at
474 a 1:6.6 ratio (w/w) for 1 h on ice.

475

476 **Electron microscopy**

477 Freshly glow-discharged, homemade, carbon-coated formvar films on copper grids (Agar
478 Scientific) were used for all EM applications. All specimens were observed using a Tecnai
479 G2 (FEI) electron microscope at an acceleration voltage of 120 kV. Images were obtained
480 using a SIS Morada digital camera and TIA software (FEI).

481 **Cage size and lattice curvature determination**

482 Samples were dialysed in assembly-promoting buffer A (100 mM MES, 1 mM EGTA, 0.5 mM
483 $MgCl_2$, 2 mM $CaCl_2$). Assembled cages were adsorbed to EM grids by placing grids on 10 µl
484 droplets of samples at 0.2 mg/ml on Parafilm for 90 s. Excessive liquid was removed using
485 filter paper and grids washed twice by transferring them sequentially onto two 15 µl droplets
486 of buffer A. Samples were then stained with 2% uranyl acetate in water for 1 min and air-
487 dried before subjected to EM analysis. Diameters of clathrin cages were measured from
488 electron micrographs using ImageJ software (NIH). Distribution of diameters was averaged
489 from the size distribution of 200 cages from three independent sets of experiments. For
490 quantification of the proportion of the two cage populations, grouped into cages smaller or
491 larger than 90nm in diameter, the proportions of the area under the curve for each population
492 and experiment were averaged and tested for statistically significant differences between
493 reconstituted clathrin isoforms using Prism 6 (GraphPad).

494

495 **Lattice assembly and quality assessment**

496 For incubation, EM grids were placed on 5-15 µl droplets on Parafilm at room temperature.
497 Grids were firstly incubated with 0.04 mg/ml tag-free epsin 1 or H_6-ΔENTH-epsin$^{144-575}$ in
498 buffer G (25 mM HEPES pH 7.2, 125 mM potassium acetate, 5 mM magnesium acetate) for
499 30 min. Unbound protein was removed by transferring grids to two droplets of buffer G before
500 incubating grids with clathrin at 0.05 mg/ml in buffer G containing 0.1% BSA for 30 min.
501 Lattices were fixed with 3% glutaraldehyde in buffer G for 15 min and stained with 2% or 5%
502 uranyl acetate in water for 1 min. Lattice regularity was assessed from electron micrographs
503 of similar quality and various focuses for each specimen as a measure of lattice quality (20).
504 For this, 2D Fast Fourier Transform (FFT) was produced using ImageJ software (NIH). The
505 height of the peak corresponding to the periodicity of the lattice (at ~0.036 nm^{-1}) served as a
506 measure for lattice quality – the higher the peak, the higher the quality of the lattice. 5-12
507 images were analysed for each reconstituted clathrin isoform within each of three
508 independent sets of experiments.

509 **In vitro budding assay**

510 *In vitro* budding was performed as previously described (48). In brief, H_6-ΔENTH-epsin$^{144-575}$
511 were bound to liposomes made from brain polar lipid extracts containing 5% DGS-Ni-NTA
512 lipids (Avanti). H_6-ΔENTH-epsin$^{144-575}$-coated liposomes were then chilled to 15°C and mixed
513 with clathrin triskelia stock solutions at 15°C, incubated for 30 min at 15°C and then
514 transferred on ice. Samples were then fixed at 4°C overnight and processed for EM analysis.
515 Diameter, coat length, budding angle and neck width of clathrin-coated membrane profiles
516 were measured from electron micrographs using ImageJ (NIH) and data processed using
517 Prism (GraphPad). Between 150 and 200 coat profiles, randomly sampled across four thin
518 sections, were analysed for each sample (> 60 000 nm total coat length per experiment per
519 sample). The proportion of curved lattices, defined by a diameter of less than 200 nm, of all
520 lattice profiles examined, was used as a measure of budding efficiency. Results from 3-5
521 independent sets of experiments were tested for statistical significance.

522

523 **Generation of CLC KO mice**

524 The *Cltb*$^{ko/ko}$ mouse strain used for this research project was created from ES cell clone
525 19159A-F4, generated by Regeneron Pharmaceuticals, Inc., and obtained from the KOMP
526 Repository (www.komp.org). Methods used to create the CLCb-null ES cell clone have
527 previously been published (66). In brief, the complete coding region of the *Cltb* gene was
528 completely deleted by homologous recombination using a large BAC-based targeting vector.
529 Targeted ES cells were then injected into albino C57BL/6J-N blastocytes and transferred into
530 foster mothers. Chimeric offspring were mated with C57BL/6J females (Charles River), and
531 germ-line transmission of the *Cltb*-null allele (*Cltb*^{ko}) was established. Heterozygote *Cltb*$^{ko/+}$
532 mice were backcrossed on the C57BL/6 background and bred to produce *Cltb*$^{ko/ko}$
533 homozygous mice. CLCa KO mice were derived from C57BL/6 WT mice (9).

534

535 **Analysis of protein expression in brain**

536 Mouse brains were harvested from six 9-12-month old C57BL/6 WT and homozygous CLCa
537 and CLCb KO mice and quickly snap-frozen in liquid nitrogen and stored at −80°C until
538 further use. Tissue were quickly thawed and homogenised in lysis buffer (50 mM HEPES
539 pH 8.0, 50 mM NaCl, 1% Triton-X 100, 5 mM EDTA, 2 mM $CaCl_2$, 1 mM PMSF, cOmplete™
540 Protease Inhibitor Cocktail mix (Roche)). The homogenate was further incubated on ice for
541 45 min before centrifugation at 21 000 g and 4°C for 2 x 10 min in an Eppendorf 5424 R
542 benchtop centrifuge (Eppendorf). Protein content of the lysate was determined by BCA assay
543 (Thermo Fisher). For analysis, 25 µg of sample were loaded on 4-15% acrylamide gels (Bio-
544 Rad) and subjected to SDS-PAGE and western blotting. Primary antibodies used for
545 immunoblotting were T.D1 (anti-CHC, made in-house), X16 (anti-CLCa, made in-house),
546 CLTB (anti-CLCb, Proteintech) and anti-beta-actin (Sigma-Aldrich).

547

548 **Electrophysiology**

549 Experiments were performed in 8-10-month-old mice. Both male and female mice were used
550 for electrophysiological experiments. Acute transverse hippocampal slices (300µm) of
551 homozygous CLCa or CLCb KO and control mice were cut on a Leica VT-1000 vibratome in
552 ice-cold artificial cerebrospinal fluid (ACSF) bubbled with 95% O_2/5% CO_2 containing (in
553 mM): NaCl (125), KCl (2.4), $NaHCO_3$ (26), NaH_2PO_4 (1.4), D-(+)-Glucose (20), $CaCl_2$ (0.5)
554 and $MgCl_2$ (3). At 5-minute intervals, slices were then transferred into a series of 3 different
555 chambers oxygenated (95% O_2/5% CO_2) in the same base ACSF but with the following
556 temperature and component (in mM) variations: **1.** 21°C initially with $MgCl_2$ (1) and $CaCl_2$
557 (0.5) then allowed to heat gradually to 36°C; **2.** 36°C with $MgCl_2$ (1) and $CaCl_2$ (1); and **3**.
558 36°C initially with $MgCl_2$ (1) and $CaCl_2$ (2) before cooling to 21°C. Slices were then left for at
559 least 1 hr before recordings commenced.

560

561 Evoked recordings were performed on an upright microscope continually perfused with
562 oxygenated recording solution at room temperature containing the same ACSF composition

as the third chamber and supplemented with 10 μM bicuculline. Pyramidal cells in the CA1 region were held at -60mV in whole-cell voltage-clamp configuration using glass microelectrodes (resistance 3-8 MΩ) filled with caesium gluconate intracellular solution containing (in mM): D-gluconic acid lactone (130), HEPES (10), EGTA (10), NaCl (10), $CaCl_2$ (0.5), $MgCl_2$(1), ATP (1) and GTP (0.5), QX314 (5), pH to 7.2 with CsOH. To evoke postsynaptic EPSCs, a bipolar concentric stimulation electrode (FHC) was placed in the SC fibres of the CA3 region. For input-output recordings, the stimulus pulse was varied between 0.2 and 1mA with a pulse width of 0.1 ms and stimuli were delivered at a rate of 0.1 Hz. Paired pulse stimuli were given at rate of 0.2 Hz with different inter-stimulus intervals, ranging from 50 ms to 200 ms and a stimulation strength set to approximately 50% of the maximal response for each cell. PPR was calculated as the ratio of the peak amplitude of the second response over the first response. Calculation of RRP size, initial fusion efficiency and SV recycling rate was done on ESPC recordings that underwent 3 s duration trains of stimulation at 20Hz and estimated as previously described (53, 67). Briefly, RRP, fusion efficiency (*fe*) and vesicle recycling rate (α) were evaluated from the cumulative charge during the stimulation train using the following two equations:

Equation 1:

$$fe = \frac{r(1)}{r(\infty)}(1 - \exp(-\alpha\Delta t))$$

Equation 2:

$$fe = \frac{r(1)}{\sum_{i=1}^{s} r(i)\exp(-\alpha(S-i)\Delta t)}$$

r(1) is the charge of the first EPSC in the train

r(i) the charge passed by the *i*th EPSC

r(∞) was calculated from the average charge of the last 10 EPSCs in the train

Δ*t* is the stimulus interval in the train

The RRP was estimated as RRP=*r*(1)/*fe*.

591 All currents were recorded using an Axopatch 200B amplifier, filtered (1 kHz) and digitised
592 (10 kHz). Data were monitored online and analysed offline using WinEDR and WinWCP
593 software (available free online at http://spider.science.strath.ac.uk/sipbs/software_ses.htm).
594 Stimulus artefacts in representative traces were digitally removed for clarity.
595

596 **Electron microscopy of synapse ultrastructure**

597 Experiments were performed in 4-12-month-old mice. Female mice were used for
598 ultrastructural experiments. Brain hemispheres were collected from homozygous KO mice
599 and WT littermates and cut in sagittal orientation. Slices were fixed in 2% paraformaldehyde
600 and 1.5% glutaraldehyde and stained sequentially with 1.5% potassium ferricyanide and 1%
601 OsO_4, 1% thiocarbohydrazide, 2% OsO4, 1% uranyl acetate, 0.66% lead nitrate in aspartic
602 acid. Samples were then gradually dehydrated and embedded for electron microscopy. The
603 ultrastructure of excitatory synapses in four electron micrographs of the VI lobule of the
604 cerebellum or CA1 hippocampus perinuclear region per genotype were analysed for the
605 ultrastructure of excitatory synapses using ImageJ (NIH) and Prism 6 (GraphPad) software
606 (n = 3). To determine SV density, SVs in 300 nm vicinity to the centre of the PSD in each
607 synapse were counted.
608

609 **Mouse behavioural tests**

610 All experiments were performed in accordance with the Animals Scientific procedures Act UK
611 (1986). Heterozygous *Cltb*$^{ko/+}$ mice were crossed to obtain homozygous *Cltb*$^{ko/ko}$ mice and
612 WT littermates. Heterozygous Clta$^{ko/+}$ mice were crossed to obtain homozygous *Clta*$^{ko/ko}$ mice
613 and WT littermates. Experiments were performed in 2-8-month-old mice. Male mice only
614 were used for all behavioural experiments.
615

616 Rotarod latency (Accelerating Rotarod; Ugo-Basile 7650 model) was used to assess motor
617 coordination. Mice were placed on the Rotarod, which was slowly accelerated from 3 to 30

618 rounds per minute over 5 minutes. Mice were given 3 trials per day for 2 days with at least 10
619 min inter-trial intervals. Time to fall from the rotarod (latency) was recorded for each trial.
620 Mice that remained on the Rotarod for the whole 5 min trial were assigned a 300 second
621 latency.
622
623 Grip strength (grip strength meter; Columbus Instruments) was used to measure muscle
624 strength in the forepaws. The grip strength meter was positioned horizontally, and mice were
625 held by the tail and allowed to grasp the metal pull-bar. The animals were then pulled back
626 and the force applied to the bar and the moment the grasp was released was recorded. Mice
627 were given 5 trials with 1 min inter-trial intervals and were tested on 2 days. The mean of
628 results from 10 trials was assigned for the grip strength of each animal.
629
630 Grid-walking was used to assess spontaneous motor deficits and limb movements involved
631 in precise stepping, coordination, and accurate paw placement. Adult mice were required to
632 navigate over a wire mesh grid. After each trial, 70% ethanol was used to clean the
633 apparatus. Mice were given 3 trials with 1 min inter-trial intervals and were tested on 2 days.
634 Behaviour on the grid was recorded on camera and was analysed later by an experimenter
635 who was blind to the genotype. A foot-slip was scored when the paw completely missed a
636 rung and the limb fell between the rungs. Counts of foot-slips for right forelimb, left forelimb,
637 right hindlimb and left hindlimb were obtained. Total footsteps were also recorded. The mean
638 of results from 10 trials was used for each animal.
639
640 **Statistical analysis**
641 All experiments were performed at least three times. All calculations and graphs were
642 performed with ImageJ, Microsoft Excel and GraphPad Prism software. P-values were
643 calculated using two-tailed Student's unpaired or paired (*in vitro* budding) t-tests, two-way
644 ANOVA with repeated measures (electrophysiology), one-way ANOVA followed by Holm-
645 Sidak correction for multiple comparison or one-way ANOVA for preselected pairs without

correction for multiple comparison (clathrin biophysical properties). Detailed statistical information including statistical tests used, number of independent experiments, *p* values and definition of error bars is listed in individual figure legends.

650 **ACKNOWLEDGMENTS**

651 This work was supported by grants to F. M. B. from the Wellcome Trust (107858/Z/15/Z), to
652 P.C.S. from the Medical Research Council (MR/M024083/1) and to P.C.S. and E. P. from
653 Alzheimer's Research UK (ARUK-PG2018A-002). L. R. was supported by a Wellcome Trust
654 4-year interdisciplinary PhD studentship. J. J. B. was supported by MRC funding to the MRC
655 Laboratory of Molecular Cell Biology at UCL, award code MC_U12266B. P. N. D. was
656 supported by a UCL Excellence Fellowship. The authors would like to acknowledge UCL
657 IQPath, UCL Institute of Neurology, Queen Square London, WC1N 3BG for processing
658 tissue slices for H&E staining and Massimo Signore (ICH) and Anna Crowley (KLB
659 Transgenic facility, UCL) for the generation of the *Cltb*^{ko} mouse strain.

660

661 **AUTHOR CONTRIBUTIONS**

662 The study was conceived by L. R. and F. M. B. with expert input from P. N. D., F. M., E. P. V.
663 and P. C. S. and the project was managed by F.M.B. Electrophysiology experiments were
664 conducted and analysed by F. M. All *in vitro* reconstitution, protein level and EM experiments
665 and analyses were carried out by L. R. with expert assistance from J. J. B., F. M., E. P. V., P.
666 N. D. and K. B. Mouse behaviour data and survival characteristics were collected by M. D. C.
667 and Y. C. The paper was written by L. R., F. M. B., F. M. and P. C. S. and then all authors
668 read and commented on the paper.

669

670 **COMPETING INTEREST**

671 The authors declare no competing interest.

672

673 **REFERENCES**

674

675 1. F. M. Brodsky, Diversity of clathrin function: new tricks for an old protein. *Annu Rev*
676 *Cell Dev Biol* **28**, 309-336 (2012).

677 2. T. Soykan, T. Maritzen, V. Haucke, Modes and mechanisms of synaptic vesicle
678 recycling. *Curr Opin Neurobiol* **39**, 17-23 (2016).

679 3. H. T. McMahon, E. Boucrot, Molecular mechanism and physiological functions of
680 clathrin-mediated endocytosis. *Nat Rev Mol Cell Biol* **12**, 517-533 (2011).

681 4. P. N. Dannhauser *et al.*, CHC22 and CHC17 clathrins have distinct biochemical
682 properties and display differential regulation and function. *J Biol Chem* **292**, 20834-
683 20844 (2017).

684 5. T. Kirchhausen *et al.*, Clathrin heavy chain: molecular cloning and complete primary
685 structure. *Proc Natl Acad Sci U S A* **84**, 8805-8809 (1987).

686 6. A. P. Jackson, H. F. Seow, N. Holmes, K. Drickamer, P. Parham, Clathrin light chains
687 contain brain-specific insertion sequences and a region of homology with
688 intermediate filaments. *Nature* **326**, 154-159 (1987).

689 7. D. E. Wakeham *et al.*, Clathrin heavy and light chain isoforms originated by
690 independent mechanisms of gene duplication during chordate evolution. *Proc Natl*
691 *Acad Sci U S A* **102**, 7209-7214 (2005).

692 8. M. Fumagalli *et al.*, Genetic diversity of CHC22 clathrin impacts its function in glucose
693 metabolism. *eLife* **8** (2019).

694 9. S. Wu *et al.*, Clathrin light chains' role in selective endocytosis influences antibody
695 isotype switching. *Proc Natl Acad Sci U S A* **113**, 9816-9821 (2016).

696 10. J. Giudice *et al.*, Alternative splicing regulates vesicular trafficking genes in
697 cardiomyocytes during postnatal heart development. *Nat Commun* **5**, 3603 (2014).

698 11. M. Mettlen *et al.*, Endocytic Accessory Proteins Are Functionally Distinguished by
699 Their Differential Effects on the Maturation of Clathrin-coated Pits. *Mol Biol Cell* **20**,
700 3251-3260 (2009).

701 12. O. M. Tsygankova, J. H. Keen, A unique role for clathrin light chain a in cell spreading
702 and migration. *J Cell Sci* 10.1242/jcs.224030 (2019).

703 13. P. H. Chen *et al.*, Crosstalk between CLCb/Dyn1-Mediated Adaptive Clathrin-
704 Mediated Endocytosis and Epidermal Growth Factor Receptor Signaling Increases
705 Metastasis. *Dev Cell* **40**, 278-288.e275 (2017).

706 14. H. Maib, F. Ferreira, S. Vassilopoulos, E. Smythe, Cargo regulates clathrin-coated pit
707 invagination via clathrin light chain phosphorylation. *J Cell Biol* **217**, 4253 (2018).

708 15. J. C. Stachowiak, F. M. Brodsky, E. A. Miller, A cost-benefit analysis of the physical
709 mechanisms of membrane curvature. *Nat Cell Biol* **15**, 1019-1027 (2013).

710 16. J. A. Ybe *et al.*, Light Chain C-Terminal Region Reinforces the Stability of Clathrin
711 Heavy Chain Trimers. *Traffic* **8**, 1101-1110 (2007).

712 17. D. S. Chu, B. Pishvaee, G. S. Payne, The Light Chain Subunit Is Required for
713 Clathrin Function in Saccharomyces cerevisiae. *J Biol Chem* **271**, 33123-33130
714 (1996).

715 18. J. D. Wilbur *et al.*, Conformation switching of clathrin light chain regulates clathrin
716 lattice assembly. *Dev Cell* **18**, 841-848 (2010).

717 19. D. H. Wong *et al.*, Neuron-specific expression of high-molecular-weight clathrin light
718 chain. *J Neurosci* **10**, 3025-3031 (1990).

719 20. P. N. Dannhauser *et al.*, Effect of clathrin light chains on the stiffness of clathrin
720 lattices and membrane budding. *Traffic* **16**, 519-533 (2015).

721 21. M. Lherbette, L. Redlingshofer, F. M. Brodsky, I. A. T. Schaap, P. N. Dannhauser,
722 The AP2 adaptor enhances clathrin coat stiffness. *FEBS J* **286**, 4074-4085 (2019).

723 22. C. Y. Chen, F. M. Brodsky, Huntingtin-interacting protein 1 (Hip1) and Hip1-related
724 protein (Hip1R) bind the conserved sequence of clathrin light chains and thereby
725 influence clathrin assembly in vitro and actin distribution in vivo. *J Biol Chem* **280**,
726 6109-6117 (2005).

727 23. J. D. Wilbur *et al.*, Actin binding by Hip1 (huntingtin-interacting protein 1) and Hip1R
728 (Hip1-related protein) is regulated by clathrin light chain. *J Biol Chem* **283**, 32870-
729 32879 (2008).

730 24. M. Biancospino *et al.*, Clathrin light chain A drives selective myosin VI recruitment to
731 clathrin-coated pits under membrane tension. *Nat Commun* 10.1038/s41467-019-
732 12855-6 (2019).

733 25. A. M. Schreij *et al.*, LRRK2 localizes to endosomes and interacts with clathrin-light
734 chains to limit Rac1 activation. *EMBO Rep* **16**, 79-86 (2014).

735 26. J. E. Heuser, T. S. Reese, Evidence for recycling of synaptic vesicle membrane
736 during transmitter release at the frog neuromuscular junction. *Journal of Cell Biology*
737 **57**, 315-344 (1973).

738 27. S. Watanabe *et al.*, Clathrin regenerates synaptic vesicles from endosomes. *Nature*
739 **515**, 228-233 (2014).

740 28. S. Watanabe, E. Boucrot, Fast and ultrafast endocytosis. *Curr Opin Cell Biol* **47**, 64-
741 71 (2017).

742 29. S. F. Soukup, R. Vanhauwaert, P. Verstreken, Parkinson's disease: convergence on
743 synaptic homeostasis. *EMBO J* **37**, e98960 (2018).

744 30. S. J. Koo *et al.*, Vesicular Synaptobrevin/VAMP2 Levels Guarded by AP180 Control
745 Efficient Neurotransmission. *Neuron* **88**, 330-344 (2015).

746 31. M. Cao *et al.*, Parkinson Sac Domain Mutation in Synaptojanin 1 Impairs Clathrin
747 Uncoating at Synapses and Triggers Dystrophic Changes in Dopaminergic Axons.
748 *Neuron* **93**, 882-896.e885 (2017).

749 32. I. Milosevic *et al.*, Recruitment of Endophilin to Clathrin-Coated Pit Necks Is Required
750 for Efficient Vesicle Uncoating after Fission. *Neuron* **72**, 587-601 (2011).

751 33. Natalia L. Kononenko *et al.*, Clathrin/AP-2 Mediate Synaptic Vesicle Reformation
752 from Endosome-like Vacuoles but Are Not Essential for Membrane Retrieval at
753 Central Synapses. *Neuron* **82**, 981-988 (2014).

754 34. Y.-I. Yim *et al.*, Endocytosis and clathrin-uncoating defects at synapses of auxilin
755 knockout mice. *Proceedings of the National Academy of Sciences* **107**, 4412 (2010).

756 35. T. Mitsunari *et al.*, Clathrin adaptor AP-2 is essential for early embryonal
757 development. *Mol Cell Biol* **25**, 9318-9323 (2005).

758 36. A. Musacchio *et al.*, Functional organization of clathrin in coats: combining electron
759 cryomicroscopy and X-ray crystallography. *Mol Cell* **3**, 761-770 (1999).

760 37. W. K. den Otter, M. R. Renes, W. J. Briels, Self-assembly of three-legged patchy
761 particles into polyhedral cages. *J Phys: Condens Matter* **22**, 104103 (2010).

762 38. A. Fotin *et al.*, Molecular model for a complete clathrin lattice from electron
763 cryomicroscopy. *Nature* **432**, 573-579 (2004).

764 39. F. Baschieri *et al.*, Frustrated endocytosis controls contractility-independent
765 mechanotransduction at clathrin-coated structures. *Nat Commun* **9**, 3825 (2018).

766 40. S. Schein, Architecture of clathrin fullerene cages reflects a geometric constraint--the
767 head-to-tail exclusion rule--and a preference for asymmetry. *J Mol Biol* **387**, 363-375
768 (2009).

769 41. F. K. Winkler, K. K. Stanley, Clathrin heavy chain, light chain interactions. *EMBO*
770 *Journal* **2**, 1393-1400 (1983).

771 42. P. K. Nandi, H. T. Pretorius, R. E. Lippoldt, M. L. Johnson, H. Edelhoch, Molecular
772 properties of the reassembled coat protein of coated vesicles. *Biochemistry* **19**, 5917-
773 5921 (1980).

774 43. P. P. Van Jaarsveld, P. K. Nandi, R. E. Lippoldt, H. Saroff, H. Edelhoch,
775 Polymerization of clathrin protomers into basket structures. *Biochemistry* **20**, 4129-
776 4135 (1981).

777 44. J. Heuser, T. Kirchhausen, Deep-etch views of clathrin assemblies. *J Ultrastruct Res*
778 **92**, 1-27 (1985).

779 45. E. Ungewickell, H. Ungewickell, Bovine brain clathrin light chains impede heavy chain
780 assembly in vitro. *J Biol Chem* **266**, 12710-12714 (1991).

781 46. B. Greene, S. H. Liu, A. Wilde, F. M. Brodsky, Complete reconstitution of clathrin
782 basket formation with recombinant protein fragments: adaptor control of clathrin self-
783 assembly. *Traffic* **1**, 69-75 (2000).

784 47. S.-H. Liu, M. L. Wong, C. S. Craik, F. M. Brodsky, Regulation of Clathrin Assembly
785 and Trimerization Defined Using Recombinant Triskelion Hubs. *Cell* **83**, 257-267
786 (1995).

787 48. P. N. Dannhauser, E. J. Ungewickell, Reconstitution of clathrin-coated bud and
788 vesicle formation with minimal components. *Nat Cell Biol* **14**, 634-639 (2012).

789 49. O. Avinoam, M. Schorb, C. J. Beese, J. A. G. Briggs, M. Kaksonen, Endocytic sites
790 mature by continuous bending and remodeling of the clathrin coat. *Science* **348**,
791 1369-1372 (2015).

792 50. B. L. Scott *et al.*, Membrane bending occurs at all stages of clathrin-coat assembly
793 and defines endocytic dynamics. *Nat Commun* **9**, 419 (2018).

794 51. S. Watanabe *et al.*, Ultrafast endocytosis at mouse hippocampal synapses. *Nature*
795 **504**, 242-247 (2013).

796 52. L. E. Dobrunz, Release probability is regulated by the size of the readily releasable
797 vesicle pool at excitatory synapses in hippocampus. *International Journal of*
798 *Developmental Neuroscience* **20**, 225-236 (2002).

799 53. J. F. Wesseling, D. C. Lo, Limit on the role of activity in controlling the release-ready
800 supply of synaptic vesicles. *J Neurosci* **22**, 9708-9720 (2002).

801 54. C. F. Stevens, J. H. Williams, Discharge of the Readily Releasable Pool With Action
802 Potentials at Hippocampal Synapses. *Journal of Neurophysiology* **98**, 3221-3229
803 (2007).

804 55. L. E. Dobrunz, C. F. Stevens, Heterogeneity of release probability, facilitation, and
805 depletion at central synapses. *Neuron* **18**, 995-1008 (1997).

806 56. R. S. Zucker, W. G. Regehr, Short-term synaptic plasticity. *Annu Rev Physiol* **64**,
807 355-405 (2002).

808 57. H. Shiotsuki *et al.*, A rotarod test for evaluation of motor skill learning. *J Neurosci*
809 *Methods* **189**, 180-185 (2010).

810 58. S. Stamm *et al.*, Clathrin light chain B: gene structure and neuron-specific splicing.
811 *Nucleic Acids Res* **20**, 5097-5103 (1992).

812 59. T. Kirchhausen, S. C. Harrison, P. Parham, F. M. Brodsky, Location and distribution
813 of the light chains in clathrin trimers. *Proc Natl Acad Sci U S A* **80**, 2481-2485 (1983).

814 60. S. R. Majeed *et al.*, Clathrin light chains are required for the gyrating-clathrin recycling
815 pathway and thereby promote cell migration. *Nat Commun* **5**, 3891 (2014).

816 61. S. L. Acton, Brodsky, F. M., Predominance of clathrin light chain LCb correlates with
817 the presence of a regulated secretory pathway. *J Cell Biol* **111**, 1419-1426 (1990).

818 62. H. Heerssen, R. D. Fetter, G. W. Davis, Clathrin Dependence of Synaptic-Vesicle
819 Formation at the Drosophila Neuromuscular Junction. *Curr Biol* **18**, 401-409 (2008).

820 63. K. Sato *et al.*, Differential requirements for clathrin in receptor-mediated endocytosis
821 and maintenance of synaptic vesicle pools. *Proc Natl Acad Sci U S A* **106**, 1139-1144
822 (2009).

823 64. V. Poupon *et al.*, Clathrin light chains function in mannose phosphate receptor
824 trafficking via regulation of actin assembly. *Proceedings of the National Academy of*
825 *Sciences* **105**, 168-173 (2008).

826 65. C. Kalthoff, J. Alves, C. Urbanke, R. Knorr, E. J. Ungewickell, Unusual Structural
827 Organization of the Endocytic Proteins AP180 and Epsin 1. *J Biol Chem* **277**, 8209-
828 8216 (2002).

66. D. M. Valenzuela *et al.*, High-throughput engineering of the mouse genome coupled with high-resolution expression analysis. *Nat Biotechnol* **21**, 652-659 (2003).

67. L. Ciani *et al.*, Wnt signalling tunes neurotransmitter release by directly targeting Synaptotagmin-1. *Nat Commun* **6**, 8302 (2015).

835 **TABLES**

836

837 *Table 1: Regulation of clathrin lattice properties by CLC isoforms*

	high					low
Lattice curvature (pentagon formation)	CLCb	CLCa	nCLCa/b	CLCa/b	nCLCa	nCLCb
Lattice quality	CLCb	CLCa	nCLCa/b	CLCa/b	nCLCa	nCLCb
Budding efficiency	CLCb	CLCa	nCLCa/b	CLCa/b	nCLCa	nCLCb

838

839

840 **FIGURE LEGENDS**

841

842 **Fig. 1**: CLCs differentially affect lattice curvature via regulation of the CHC knee. **a** Pucker
843 (1) and knee (2) angles of the clathrin triskelion (black: CHC, blue: CLC) dictate lattice
844 architecture. Different knee angles (encircled, black straight and dashed lines) are adopted
845 for hexagon (non-curvature inducing) or pentagon (curvature inducing) formation (3, whole
846 triskelion in black and parts of others in grey). Lattice curvature is further amended through
847 changes in pucker angle (4, dashed and black lines), or changes in proximal leg-crossing
848 angle (5). CLC subunits are omitted for simplicity. Different sizes of closed cages are
849 achieved by varying numbers of hexagons and a fixed number of 12 pentagons (filled black,
850 based on (44)). **b** Quantification of the percentage of small cages (< 90 nm in diameter) of >
851 200 cages, generated by *in vitro* assembly of clathrin reconstituted with indicated CLCs, 1:1
852 mixtures of reconstituted clathrins (CLCa/b or nCLCa/b) or CHC only (CHC), determined
853 from electron micrographs (mean ± SEM, *$P < 0.05$, ***$P < 0.001$ one-way ANOVA followed
854 by Holm-Sidak correction for multiple comparison, n = 3). **c** Cage size distributions from
855 assemblies as described in **b**. **d** Size distributions of cages formed from TDD (black) and
856 Hub (grey) co-assemblies, with Hub fragments reconstituted or not with the different CLC
857 isoforms or 1:1 mixtures thereof. **e** Representative EM images of cages formed from full-
858 length CHC (top) or Hub/TDD fragments (bottom) without or following reconstitution with CLC
859 isoforms. Scale bar: 100 nm.

860

861 **Fig. 2**: CLC splicing and mixing affects *in vitro* lattice properties. **a** Clathrin reconstituted with
862 indicated CLC isoforms and mixtures thereof were assembled into flat lattices and visualised
863 by negative stain for EM analysis. Scale bar: 200 nm. **b** Quality (regularity quantified by
864 Fourier transform) of lattices generated as in **a**, (mean ± SEM, *$P < 0.05$, **$P < 0.01$, one-
865 way ANOVA followed by Holm-Sidak correction for multiple comparison, n = 5). **c** Differences

866 in lattice quality between indicated reconstituted clathrins in individual experiments as in **b**
867 (data points and mean ± SEM, n = 5).
868
869 **Fig. 3**: CLC splicing and mixing affects *in vitro* lattice budding efficiency. **a** Representative
870 EM images of clathrin reconstituted with indicated CLC isoforms, 1:1 mixtures thereof, CHC
871 only (CHC) and tissue-derived clathrin (native) assemblies on H_6-ΔENTH-epsin$^{144-575}$-coated
872 liposomes. Scale bar: 200 nm. **b** Quantification of the percentage of curved lattices (defined
873 as coats with < 200 nm fitted diameter) of > 60 000 nm total coat profiles generated as in **a**
874 (mean ± SEM, *P < 0.05, **P < 0.01, paired Student's t-test for native and CHC, n = 3, one-
875 way ANOVA with repeated measures for CLC-reconstituted clathrin, n = 4). **c** Differences in
876 percentage of curved lattices between indicated reconstituted clathrins in individual
877 experiments in **b** (data points and mean ± SEM, n = 4). **d** Quantification of budding efficiency
878 (% curved lattices determined as in **b**, normalised to native) of reconstituted clathrins and
879 mixtures thereof (*P < 0.05, one-way ANOVA for sets of neuronal or non-neuronal samples,
880 followed by Holm-Sidak correction for multiple comparison, n = 3). **e** Parameters
881 characterising coated buds (top); coat length *c*, membrane bud diameter *d*, neck width *n*, and
882 budding angle θ. Models of clathrin-mediated membrane deformation by transitional
883 curvature generation and lattice rearrangement (middle) or lattice growth under constant
884 lattice curvature (bottom). **f** Representative coat profiles for flat (left), curved (middle) and
885 budded (right) structures. **g** to **i** Analysis of the dataset generated as shown in **a** for bud
886 parameters *d* (**g**), *c* (**h**) and *n* (**i**) as shown in **e** in relation to the θ of each structure measured
887 for all reconstituted clathrins within the same experiment. Inserts in **g** and **h** show the
888 different correlations of these parameters as predicted according to the curvature transition
889 (red, straight line) constant curvature models (red, dashed line) shown in **e**.
890
891 **Fig. 4:** CLC composition regulates SV pool replenishment in hippocampal neurons. **a**
892 Immunoblot of CLC KO and WT brain lysate for CHC (TD.1 antibody), CLCa (X16 antibody),

893 CLCb (CLTB antibody) and actin (anti-beta-actin antibody). **b** Schematic illustration of
894 stimulating and recording electrode setup in hippocampal slices. The synapses investigated
895 are formed by a Schaffer-collateral (SC) axon (black) from a pyramidal neuron (black
896 triangles, cell bodies) in the CA3 region synapsing with a receiving pyramidal neuron (grey
897 triangle, cell body) in the CA1 region from which responses are recorded. Black circles
898 denote dentate gyrus (DG) granule cell bodies. **c** Representative traces of EPSCs following a
899 20 Hz electrical stimulation for 3 s in CLCa KO and WT hippocampal slices (left). Graphs
900 (right) show the mean (± SEM) initial fusion efficiency, recycling rate and readily releasable
901 pool (RRP) size calculated for all cells (n = 9-11 slices from 3 animals/genotype; $*P < 0.05$
902 and $**P < 0.01$, unpaired Student's t-test). **d** Representative traces of EPSCs following a 20
903 Hz electrical stimulation for 3 s in CLCb KO and WT hippocampus slices (left). Graphs (right)
904 show the mean (± SEM) initial fusion efficiency, recycling rate and RRP size calculated for all
905 cells (n = 11-12 slices from 4 animals/genotype; $*P < 0.05$, unpaired Student's t-test)**. e**
906 Representative EM images of excitatory synapses in the CA1 region of the hippocampus of
907 CLCa WT, CLCa KO, CLCb WT and CLCb KO. Scale bars; 300 nm. **f** to **m** Quantification of
908 data extracted from EM images as in **e**. Graphs show SV density within 300 nm of the PSD
909 (**e** and **i**), cumulative frequency distribution of SV size (**g** and **k**), postsynaptic density (PSD)
910 length (**h** and **l**) and synapse density (**i** and **m**) expressed as mean ± SEM ($*P < 0.05$,
911 unpaired Student's t-test, n = 3).
912
913 **Fig. 5**: Neuronal defects are compensated for in CLCb KO but not CLCa KO mice. **a** Input-
914 output relationship of evoked excitatory postsynaptic currents (EPSCs) at CA1 synapses of
915 WT and CLCa KO hippocampus slices. Traces show responses of representative cells at
916 increasing stimulus intensity with an average of 3 responses for each stimulus strength
917 (mean ± SEM; n = 9-11 slices from 3 animals/genotype; $*P < 0.05$, two-way ANOVA with
918 repeated measures). **b** Input-output relationship of evoked EPSCs at CA1 synapses of WT
919 and CLCb KO hippocampus slices. Traces show response of representative cells at

920 increasing stimulus intensity with an average of 3 responses for each stimulus strength
921 (mean ± SEM; n = 12-15 slices from 3 animals/genotype; *$P < 0.05$, two-way ANOVA with
922 repeated measures). **c** Paired-pulse ratio (PPR) of evoked EPSCs at CA1 synapses of WT
923 and CLCa KO hippocampal slices. Traces show responses of representative cells. Graph
924 displays the mean PPR (P_2/P_1 ± SEM) from all cells (n = 9-11 slices from 3
925 animals/genotype) at different time intervals between paired pulses (***$P < 0.001$, unpaired
926 Student's t-test). **d** PPR of EPSCs at CA1 synapses of WT and CLCb KO hippocampal
927 slices. Traces show responses of representative cells. Graph displays the mean PPR (P_2/P_1
928 ± SEM) from all cells (n = 12-15 slices from 4 animals/genotype) at different time intervals
929 between paired pulses. **e** Genotype distribution for CLCa KO (n = 590) and CLCb KO (n =
930 359) mice after weaning compared to expected distribution (****$P < 0.0001$, *Chi*-square test).
931 **f** Performance in the accelerated rotarod test (latency to fall) by CLC KO (CLCa KO = 8,
932 CLCb KO = 8) and control wild-type littermates (CLCa WT = 8, CLCb WT = 7) expressed as
933 data points and mean ± SEM (****$P < 0.0001$, unpaired Student's t-test). **g** Time to cross grid
934 for CLCa KO (n = 10) and control mice (n = 10) expressed as data points and mean ± SEM
935 (*$P < 0.05$, unpaired Student's t-test). **h** Grip strength of CLCa KO (n = 10) and control mice
936 (n = 11, gram-force relative grip strength over body weight) expressed as data points and
937 mean ± SEM.
938
939 **Fig. 6:** Model of how neuronal CLC diversity regulates synaptic vesicle recycling and lattice
940 properties. **a** CLC (cyan) neuronal splice inserts (arrowheads) are located near the TxD of
941 the bound CHC (green, left, PDB: 3LVH). **b** CLC (cyan) neuronal splice inserts (stars) are
942 near the CHC knee of the neighbouring triskelion (red or orange) within lattices (right, PDB:
943 3IYV). Interaction between a neuronal splicing insert and the knee of an adjacent triskelion
944 and/or adjacent CLC N-terminus (N) could promote conformational change in the CHC knee.
945 As the formation of pentagons and hexagons requires different knee angles, this interaction
946 could consequently influence lattice curvature (see Fig. 1a). **c** In WT mice (centre), a mix of

947 nCLCa and nCLCb clathrin creates the appropriate biophysical properties to mediate SV
948 generation from endosomal compartments (and possibly the plasma membrane, blue-green
949 arrows). Loss of nCLCa (left) creates nCLCb clathrin lattices that are defective in efficient SV
950 regeneration (blue arrows), resulting in decimated SV pools. Loss of nCLCb (right) creates
951 nCLCa clathrin lattices, which are also less efficient in SV regeneration than WT, but able
952 maintain an overall increased SV pool by excess budding to compensate for reduced acute
953 SV pool replenishment efficiency (green arrows).
954

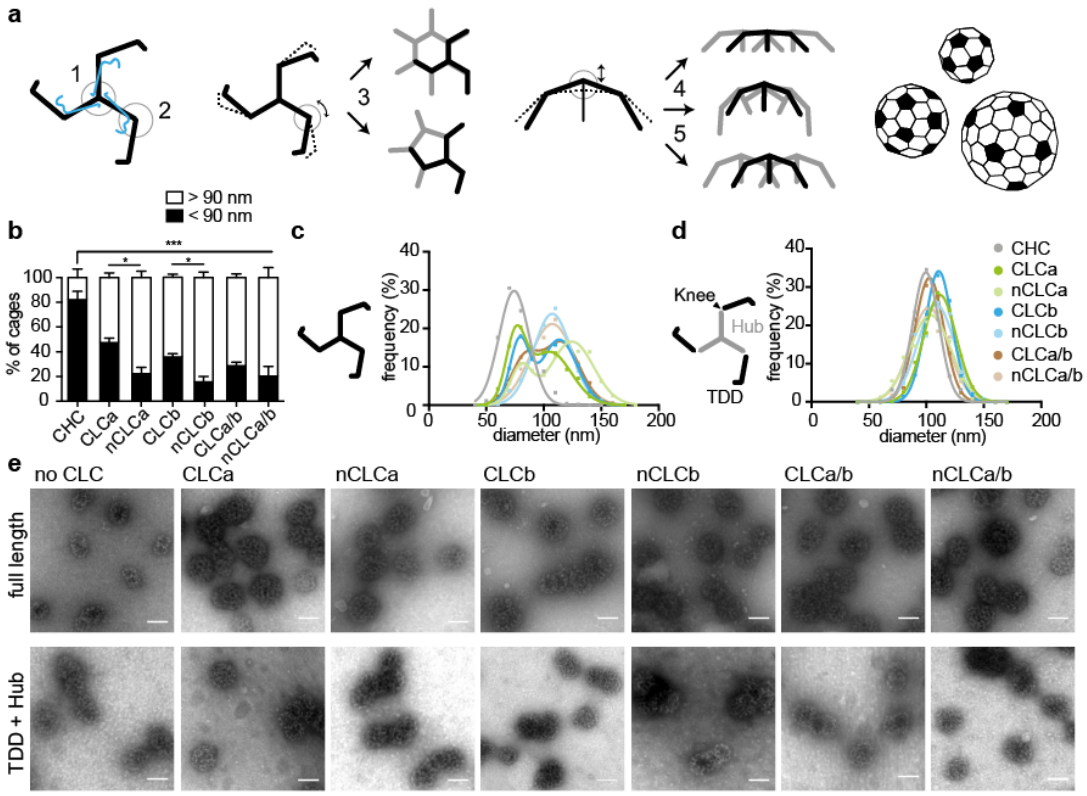
a
1
2
3
4
5
b
> 90 nm
< 90 nm
% of cages
CHC
CLCa
nCLCa
CLCb
nCLCb
CLCa/b
nCLCa/b
c
frequency (%)
diameter (nm)
d
Knee
Hub
TDD
CHC
CLCa
nCLCa
CLCb
nCLCb
CLCa/b
nCLCa/b
e
no CLC
CLCa
nCLCa
CLCb
nCLCb
CLCa/b
nCLCa/b
full length
TDD + Hub

Figure 1

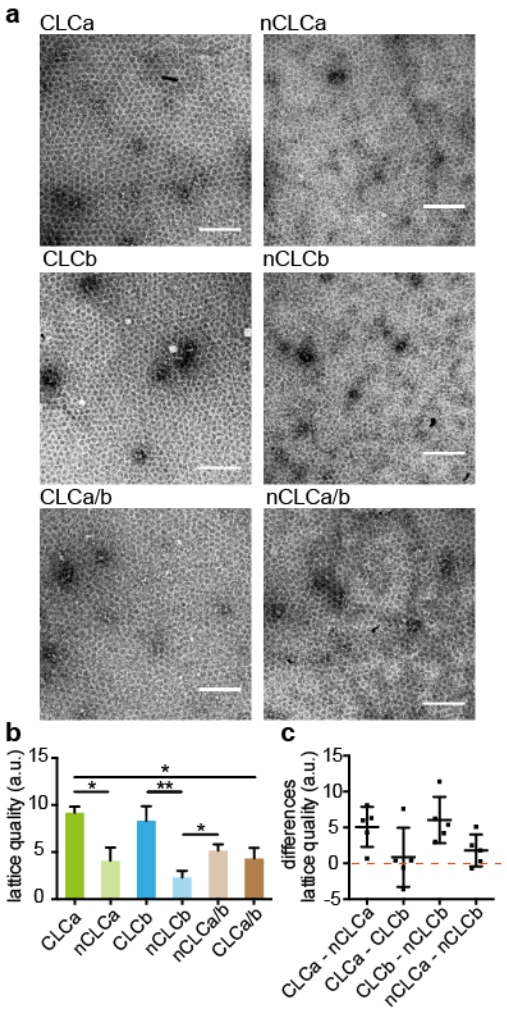
a
CLCa
nCLCa
CLCb
nCLCb
CLCa/b
nCLCa/b
b
lattice quality (a.u.)
15
10
5
0
*
**
*
*
CLCa
nCLCa
CLCb
nCLCb
nCLCa/b
CLCa/b
c
differences
lattice quality (a.u.)
15
10
5
0
-5
CLCa - nCLCa
CLCa - CLCb
CLCb - nCLCb
nCLCa - nCLCb

Figure 2

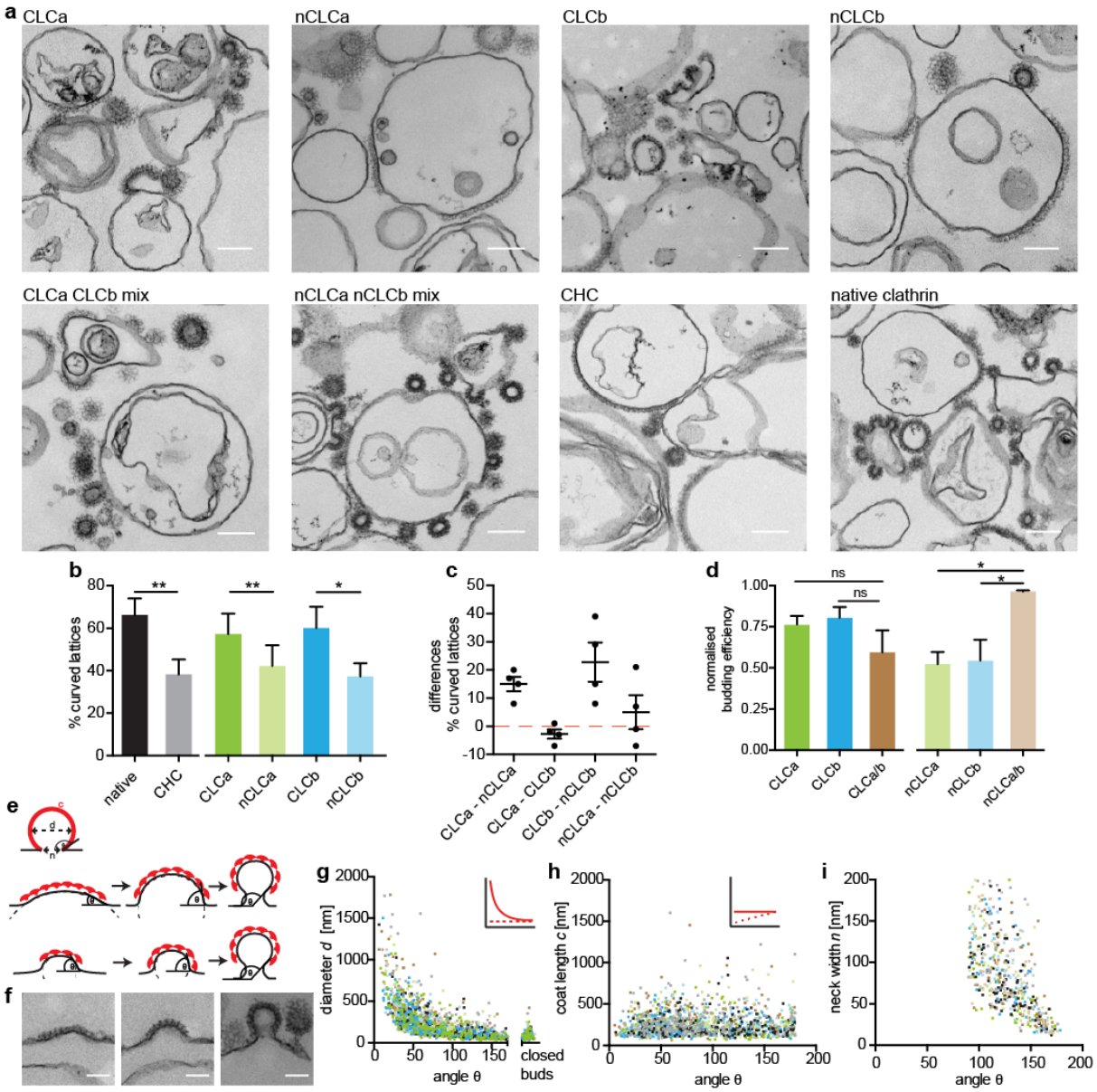
a
CLCa
nCLCa
CLCb
nCLCb
CLCa CLCb mix
nCLCa nCLCb mix
CHC
native clathrin
b
% curved lattices
native
CHC
CLCa
nCLCa
CLCb
nCLCb
c
differences % curved lattices
CLCa - nCLCa
CLCa - CLCb
CLCb - nCLCb
nCLCa - nCLCb
d
normalised budding efficiency
ns
CLCa
CLCb
CLCa/b
nCLCa
nCLCb
nCLCa/b
e
f
g
diameter d [nm]
angle θ
closed buds
h
coat length c [nm]
angle θ
i
neck width n [nm]
angle θ

Figure 3

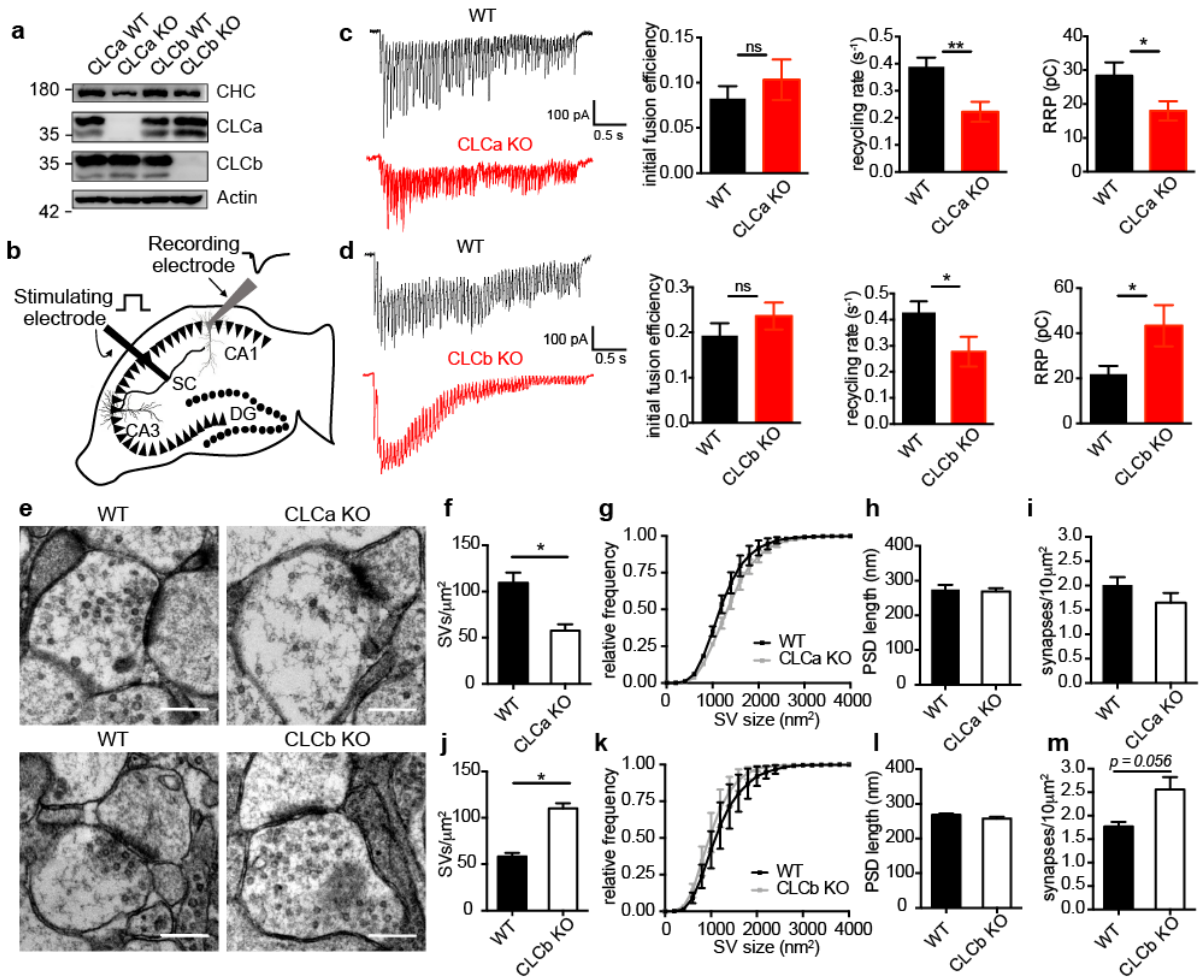
a
CLCa WT
CLCa KO
CLCb WT
CLCb KO
180
CHC
35
CLCa
35
CLCb
42
Actin
b
Recording electrode
Stimulating electrode
CA1
SC
DG
CA3
c
WT
100 pA
0.5 s
CLCa KO
initial fusion efficiency
ns
recycling rate (s-1)
**
RRP (pC)
*
d
WT
100 pA
0.5 s
CLCb KO
e
WT
CLCa KO
WT
CLCb KO
f
SVs/µm2
g
relative frequency
SV size (nm2)
WT
CLCa KO
h
PSD length (nm)
i
synapses/10µm2
j
k
l
m
p = 0.056

Figure 4

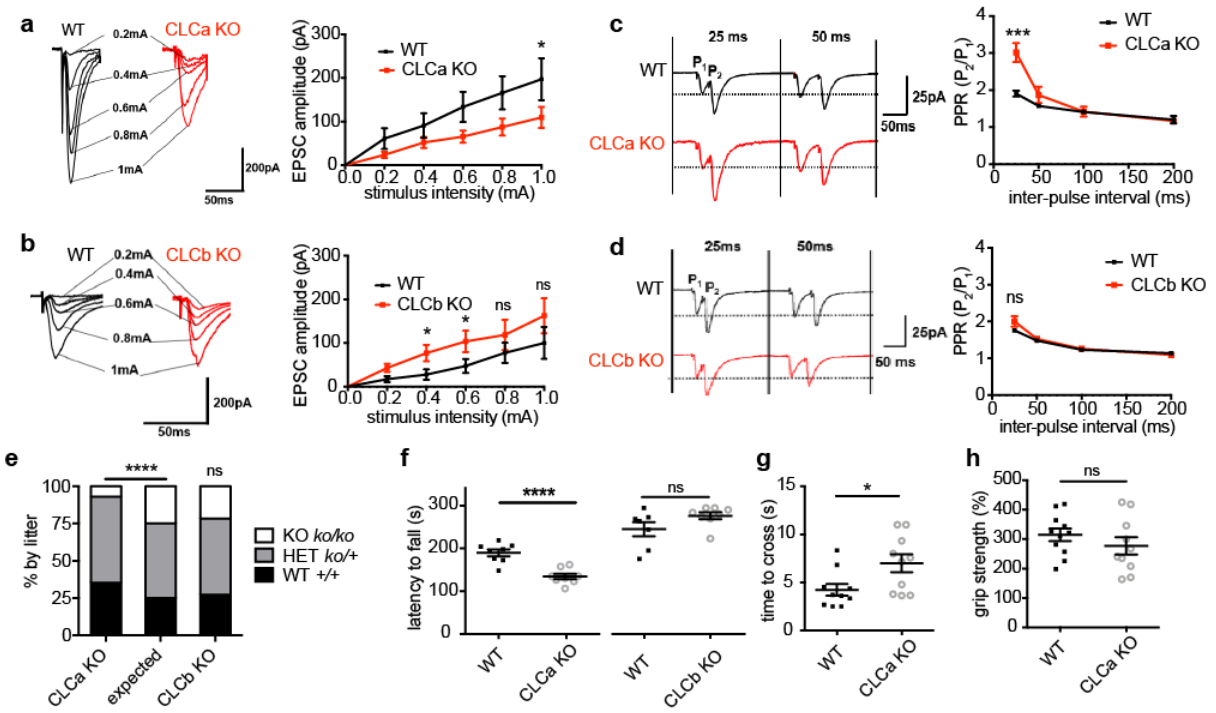
a
WT
CLCa KO
0.2mA
0.4mA
0.6mA
0.8mA
1mA
200pA
50ms
EPSC amplitude (pA)
stimulus intensity (mA)
WT
CLCa KO
b
CLCb KO
ns
c
25 ms
50 ms
25pA
50ms
PPR (P2/P1)
inter-pulse interval (ms)
d
25ms
50ms
50 ms
e
% by litter
KO ko/ko
HET ko/+
WT +/+
expected
f
latency to fall (s)
CLCb KO
g
time to cross (s)
h
grip strength (%)

Figure 5

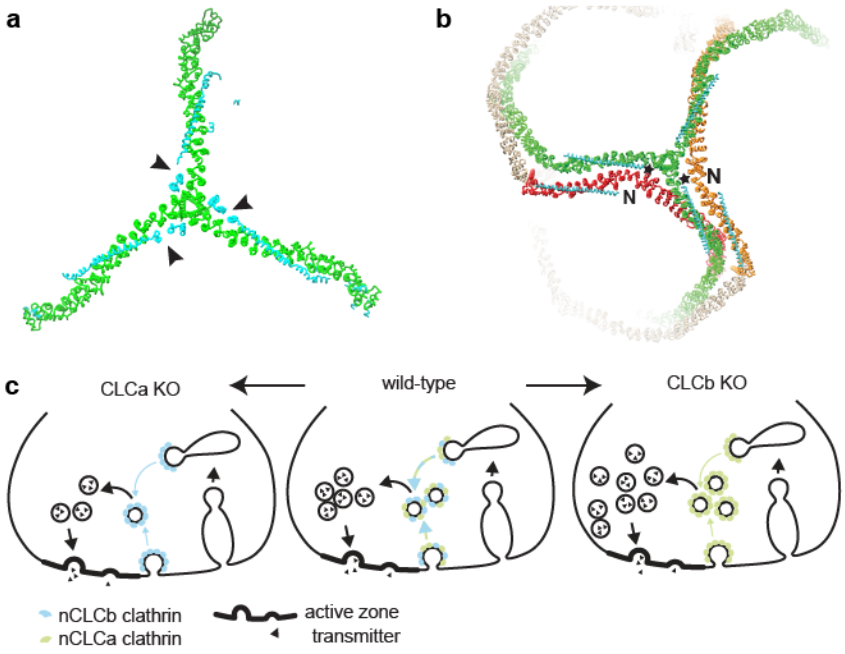

967

968 **Figure 6**